RSC Advances

PAPER

View Article Online
View Journal | View Issue

Cite this: *RSC Adv.*, 2026, **16**, 28627

Synthesis of porous aluminate microbeads from emulsion droplets: interphase alcohol extraction-driven assembly of sub-10 nm nanoparticles

Shogo Kuroda, Mei Ito, Kohji Ohno, Atsushi Nakahira and Yasuaki Tokudome *

Received 21st April 2026
Accepted 18th May 2026

DOI: 10.1039/d6ra03388a

rsc.li/rsc-advances

Porous microbeads containing inorganic nanoparticles have attracted considerable attention because they can be endowed with functionalities derived from the metal elements. One representative method for synthesizing porous microbeads containing inorganic nanoparticles is the emulsion method. Here, we develop a novel synthesis concept for the synthesis of pure inorganic porous microbeads using an aluminate system as a model system. The obtained microbeads showed microporosity with a high specific surface area as well as a spherical shape. Porous aluminate microbeads are synthesized by preparing water in oil emulsion droplets using a concentrated dispersion of aluminum hydroxide nanoparticles surface-modified with acetylacetone, followed by destabilizing the nanoparticles by extraction of alcohol from the aqueous droplets to the oil phase. We found that amphiphilic ethanol spontaneously extracted to the oil phase from the aqueous phase, destabilizing the nanoparticles and resulting in porous microbeads.

Introduction

Porous spherical particles with diameters in the μm range and pores in the nm range are attractive due to their high specific surface areas and controllable architectures of pores and spherical shape. These porous microbeads have been used in a wide range of applications, such as catalysis, gas sensing, gas adsorption, biomedical, drug delivery, electromagnetic wave absorption, electrochemical, and electromagnetic interference shielding.[1–8]

Porous microbeads containing inorganic nanoparticles are especially promising because they can be endowed with functionalities derived from the metal elements, such as magnetic responsiveness and catalytic activity.[9,10] One representative method for synthesizing porous microbeads containing inorganic nanoparticles is the emulsion method. The emulsion method involves mixing two immiscible solvents, *i.e.* aqueous and oil phases, to disperse one into the other as droplets, allowing for the synthesis of materials under relatively mild conditions. The emulsion method includes: (1) pickering emulsion method, which uses solid nanoparticles instead of surfactants to synthesize stable emulsions and (2) polymerization methods with organic polymers or silica as polymer matrixes.[11–15] Nevertheless, high loading of inorganic nanoparticles into the porous microbeads is restricted by these processing methods.

To achieve pure porous inorganic microbeads *via* emulsion method, two synthesis approaches starting from inorganic nanoparticle dispersions have been reported: (1) evaporation-driven assembly and (2) gelation-driven assembly of nanoparticles. Evaporation-driven assembly involves destabilizing the nanoparticles in the aqueous phase by evaporating the solvent inside the emulsion droplets.[16–18] Gelation-driven approach involves adding a third component, such as salt (electrolyte), to the aqueous droplets to destabilize nanoparticles by shielding the surface charge of the inorganic nanoparticles.[16,19] However, there are no examples of inorganic porous microbeads other than those based on silica (SiO_2) and titania (TiO_2). This is due to the low dispersion stability of general inorganic nanoparticles in solvents. Silica and titania are known to exhibit exceptionally-high dispersion stability in aqueous solvent even without the use of surface modifiers thanks to strong solvation of the nanoparticles.[20,21] Recently, we have reported concentrated dispersions of sub-10 nm hydroxide nanoparticles modified with small organic molecules, such as acetylacetone (acac) in various systems.[22–27] While conventional nanoparticles tend to aggregate in concentrated systems, the hydroxide nanoparticles are stabilized as concentrated dispersions due to their unique solvation state.[28] Inorganic microbeads of various chemical compositions are expected to be achieved by using these nanoparticle dispersions. Since the solvent of the concentrated dispersions of hydroxide nanoparticles is a mixture of water and alcohols, the extraction of the alcohols from aqueous phase to oil phase to destabilize the system is expected to achieve microbeads formation. As a model

Department of Materials Science, Graduate School of Engineering, Osaka Metropolitan University, Sakai, Osaka 599-8531, Japan. E-mail: tokudome@omu.ac.jp

system, we focus on the aluminate to demonstrate the concept of the current material synthesis of inorganic microbeads.

Herein, we report the synthesis of porous aluminate microbeads *via* alcohol extraction-driven assembly of hydroxide nanoparticles in emulsion droplets. This study focuses on aluminates to validate the proposed synthesis concept for inorganic microbeads. Although a similar concept of solvent–evaporation-driven assembly of organically-modified nanocrystals in o/w emulsion systems has been reported for constructing superlattices of the nanocrystals,[29] the resulting materials are typically dense spheres lacking accessible porosity. In contrast, our alcohol-extraction-driven approach enables the formation of an accessible porosity with a high specific surface area of 430 m^2 g^{-1}.

Experimental

Chemicals

Aluminum chloride hexahydrate ($AlCl_3 \cdot 6H_2O$, 98%), ethanol (>99.5%), methanol (>99.5%), 1-propanol (>99.5%), 1-butanol (>99%), dodecane (>99%), toluene (>99.5%) and acetylacetone (acac. >99%) were purchased from FUJIFILM Wako Pure Chemicals Industries. Propylene oxide (>99%) was also purchased from Sigma-Aldrich Co and 2-butanone (>99%) was also purchased from Kanto Chemical Co., Inc. In addition, poly(lauryl methacrylate)-*b*-poly(poly(ethylene glycol) methacrylate) ($PLMA_{50}$-*b*-$PPEGMA_5$) block copolymer (M_n = 11 700 g mol^{-1}) was kindly supplied by Dainichiseika Color and Chemicals Mfg. Co., Ltd, Japan. All of the chemicals were used as received.

Synthesis of aluminum hydroxide dispersion

$AlCl_3 \cdot 6H_2O$ (3.018 g, 12.5 mmol) was dissolved in a mixture of ethanol (15.00 mL, 257.25 mmol) and ion exchanged water (10.00 mL, 555.5 mmol), followed by the addition of acac (0.428 mL, 4.12 mmol). After the mixture was stirred for >30 min in a closed glass container at room temperature (25 °C), propylene oxide (13.10 mL, 185.0 mmol) was added all at once under stirring and the mixture was stirred for a further 24 h to yield a homogeneous solution. After 24 h since the addition of propylene oxide, obtained transparent dispersion of aluminum hydroxide was used for the microbeads synthesis as follows.

Preparation of porous aluminate microbeads

Porous aluminate microbeads were prepared *via* a three-step process as described in Fig. 1: (1) emulsification, (2) extraction of ethanol, and (3) washing and drying. 4.5 mL of the nanoparticles dispersion synthesized according to the section of "Synthesis of aluminum hydroxide dispersion" was added to a mixed solution of dodecane (10.00 mL, 44.0 mmol) and PLMA-*b*-PPEGMA (0.45 g) under stirring at 500 rpm and further stirred for 10 s in a closed glass container. The mixture was stirred at 2000 rpm for a further 10 min with a propellerless planetary mixer (AR-100, Thinky Co., Ltd, Japan) for emulsification. The emulsion was then allowed to stand for >6 h at 40 °C in a closed glass container (aging step). While aging, ethanol was extracted from the aqueous phase to the oil phase spontaneously. The resulting microbeads formed in the aqueous phase of the emulsion was collected and washed by centrifugation with 2-butanone, then dried under vacuum at 40 °C.

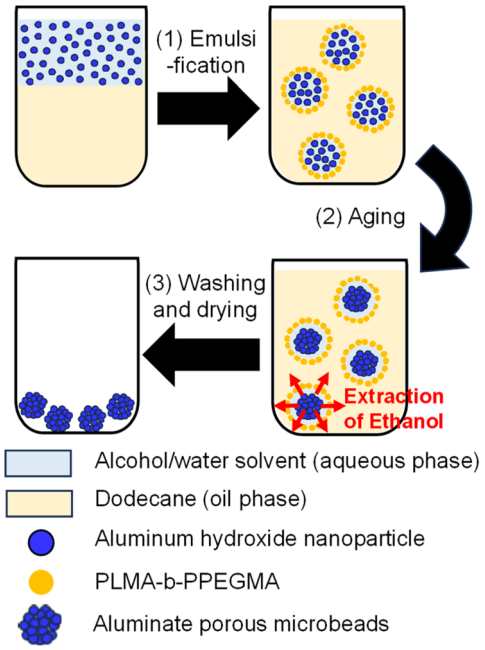

Fig. 1 Synthesis steps of porous aluminate microbeads.

Characterization

The crystallinity of samples was identified by X-ray diffraction (XRD; Mini Flex 600C, Rigaku, Corporation) using Cu Kα radiation (λ = 0.1540 nm) equipped with a one dimensional high-speed detector (D/tex Ultra2, Rigaku Corporation). The divergence slit was set to 0.625°. A Ni filter was used to remove Cu Kβ radiation. Particle morphology was observed by a transmission electron microscopy (TEM; JEM2000FX microscope, JEOL Ltd, Japan) at an accelerating voltage of 200 kV and a magnification of 100 K. For the TEM observation, the samples were dispersed in ethanol. The dispersions were then dropped onto a Cu grid (HRC-C10 STEM Cu100P, OHKEN Co., Ltd). Analysis of microbeads structure was conducted by scanning electron microscopes (SEM; JCM-7000, JEOL Ltd, Japan, and JSM-IT500HR, JEOL, Japan). A thin Pt–Pd coating was applied to the samples using an ion sputter (JFC-1100E, JEOL Ltd, Japan) to avoid charge up during observation. Emulsion droplets were examined under optical microscope (OM; HM-200, Mitutoyo Co., Ltd, Japan) with maximum magnification of 50×. Droplets were placed between glass slides before observations and photographed by a microscopy camera (WRAYCAM-EL510, WRAYMER Co., Ltd, Japan). The Fourier-transform infrared (FT-IR) spectra of the samples was recorded with a FT/IR-4600 spectrophotometer (JASCO Corporation) at a scan resolution of 4.0 cm^{-1}. For the measurement of aluminum hydroxide nanoparticle dispersion, the sample powder obtained by drying was placed between KBr plates and pressed into a pellet. Other

liquid samples were placed onto the ATR crystal and analyzed. Specific surface areas and pore size distributions of the porous microbeads were determined by N_2 adsorption–desorption isotherms using a BELSORP MINI X instrument (MICROTRAC BELL Co., Ltd, Japan). Samples were de-gassed for 24 h at 200 °C before measurement. Specific surface areas were calculated by the Brunauer–Emmett–Teller (BET) method and the pore size distributions were obtained from the adsorption branches of the isotherms using the Barrett–Joyner–Halenda (BJH) method.

Results and discussion

Preparation of aluminum hydroxide nanoparticle dispersion and porous aluminate microbeads

Concentrated (8.3 wt%) dispersion of aluminum hydroxide nanoparticles was obtained in 24 h since the addition of propylene oxide to the starting solution (Fig. 2a). Propylene oxide induces alkalization, *i.e.*, pH increase, through the ring-opening reaction of epoxide ring to form aluminum hydroxide.[30] Fig. 2b and c show a TEM image and the corresponding size distribution of aluminum hydroxide nanoparticles dried from the dispersion. The nanoparticles have a mean diameter of 5.8 nm (standard deviation: 1.5 nm). The size is small enough as a nanobuilding block for microbeads. The aggregation of aluminum hydroxide nanoparticles on TEM grid was not observed, suggesting high dispersion stability of the aluminum hydroxide in the solvent upon drying. This feature is also favorable for the homogenous synthesis of aluminate microbeads. Fig. 2d shows the XRD pattern of the dried powder of aluminum hydroxide nanoparticle dispersion. The broad peaks can be ascribed to pseudoboehmite though there is a possibility of contamination of other polymorphs of aluminum oxyhydroxide and aluminum hydroxide.[31] Fig. 2e shows the FT-IR spectrum of the dried powder obtained from the aluminum hydroxide nanoparticle dispersion. The absorption band of the overlapped peaks originating from the lattice vibration modes of Al–OH was observed at 500–1000 cm^{-1}.[32] The band at 3000–3700 cm^{-1} is derived from the stretching vibration of water molecules and the superposition of O–H stretching bands.[33–35] The peaks of the acac vibrations appear in the range of 900–1700 cm^{-1} and 2900–3000 cm^{-1}: C–C vibration at 936 cm^{-1}, C–OH vibration at 1030 cm^{-1} and C–H vibration at 1293, 1398, 2925 and 2968 cm^{-1}.[36,37] The two separate vibrations of C═O, the keto and enol forms, at 1599 and 1533 cm^{-1} reflect the chelation of acac to metal centers.[38] These results indicate that aluminum hydroxide nanoparticles are modified with acac.

Subsequently, the aluminum hydroxide colloidal dispersion (4.5 mL) was stirred with a mixed solvent of 10 mL of dodecane and 0.45 g of PLMA-*b*-PPEGMA, and then aged at 40 °C. Fig. 3a shows an optical micrograph image of the resulting emulsion droplets after aging for 10 min at 40 °C. Droplets with a wide range of sizes (5–30 μm) were observed. After centrifugation and vacuum drying of emulsion droplets, porous aluminate microbeads were obtained. Fig. 3b shows a SEM image of microbeads. The average particle size of the microbeads was 7.5 μm (standard deviation: 4.3 μm). Fig. 3c shows the N_2 adsorption–

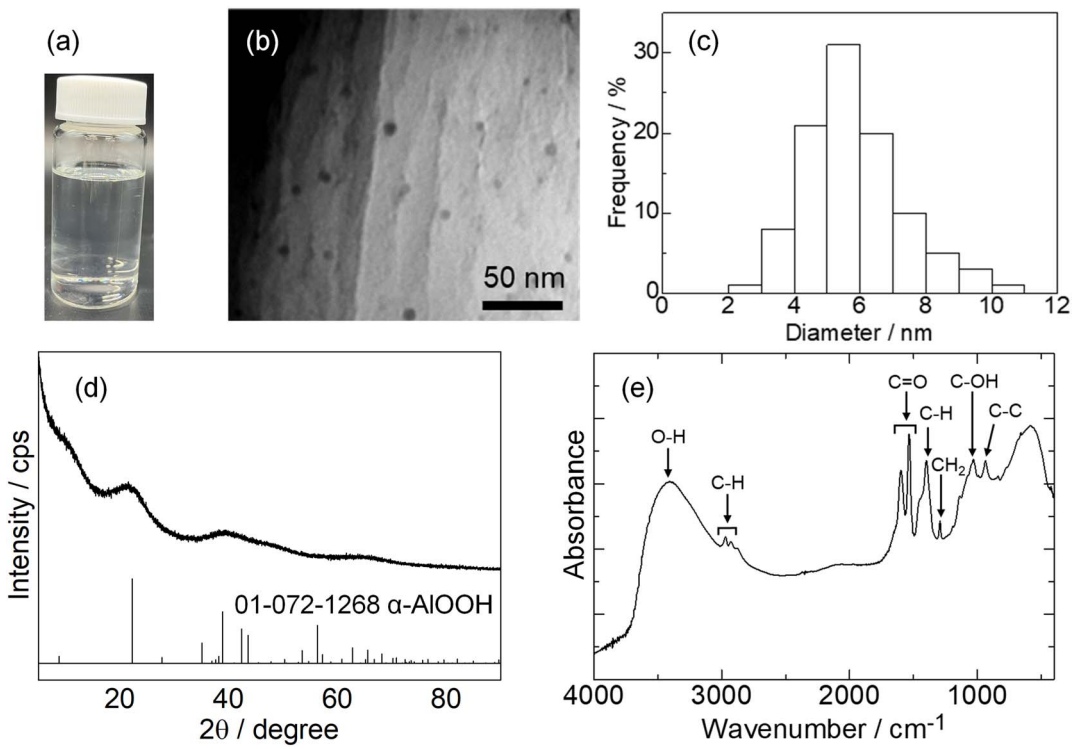

Fig. 2 (a) Appearance of aluminum hydroxide nanoparticle dispersion. (b) TEM image and (c) corresponding particle size distribution of aluminum hydroxide nanoparticles. (d) XRD pattern and (e) FT-IR spectrum of the dried powder obtained from the aluminum hydroxide dispersion.

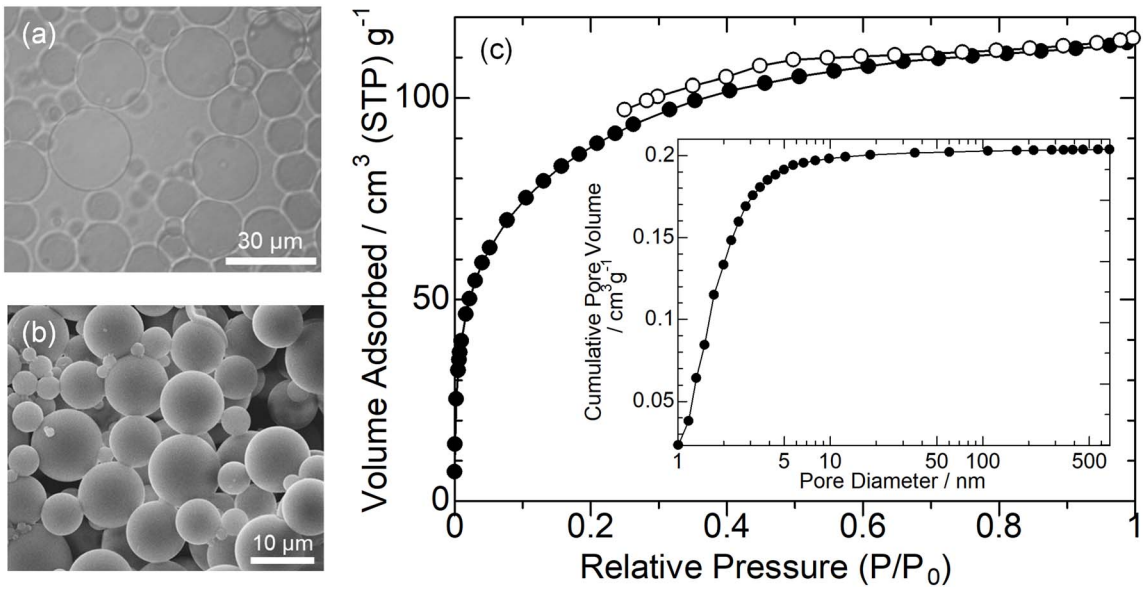

Fig. 3 (a) Optical micrograph of emulsion droplets. (b) SEM image of aluminate microbeads. (c) Nitrogen adsorption–desorption isotherms and corresponding pore size distribution curve (inset) of aluminate microbeads.

desorption isotherm and BJH pore size distribution curve of microbeads. The type I isotherm suggests the presence of micropores originating from the interstices among the primary aluminum hydroxide particles. The average pore diameter of 1.8 nm calculated from BJH method is in good agreement with the micropore size as interparticle pores considering the size of primary particles, 5.8 nm. As a result, the BET specific surface area of microbeads was as high as 430 m^2 g^{-1}. The specific surface area is determined by the size of the primary particles, similar to the behavior of xerogels derived from discrete nanoparticle dispersions.[39] We can conclude that the porous aluminate microbeads show microporosity with a high specific surface area as well as a spherical shape.

The parameter influencing the morphology of porous aluminate microbeads

The shape and the size of microbeads depend on the temperature at which alcohol extraction occurs. This was verified by comparing the temperature of aging (25–80 °C). Fig. 4a shows the SEM image of microbeads synthesized at 25 °C. The average particle size was 2.9 μm (standard deviation: 2.01 μm). Increased fraction of smaller microbeads was observed compared to the case of 40 °C (Fig. 3b). Fig. 4b–d show SEM images of microbeads synthesized at 50, 60 and 80 °C. The microbeads aged at 50 °C show an average particle size of 7.4 μm (standard deviation: 3.9 μm) and the shape comparable to that at 40 °C. The shape of microbeads was in part irregular after aging above at 60 °C. Most microbeads show irregular shapes with being connected each other after aging at 80 °C. These results suggest that the diffusion rate of ethanol increases as the temperature increases, causing excessive extraction of ethanol and making the emulsion unstable. Optical micrographs (Fig. S1) suggest that the movement of droplets is slow at 25 °C and the frequency of coalescences between droplets is relatively low. We also found that the shape and particle size of microbeads depend on the composition of the dispersion and the type of alcohol used for the synthesis of aluminum hydroxide dispersion (Fig. S2 and S3). The synthesis parameters of microbeads need to be optimized to obtain spherical aluminate microbeads. Generally, the structures of porous materials depend on drying conditions form corresponding wet gels.[39,40] While the present study employed vacuum drying at 40 °C, varying these conditions or utilizing supercritical drying could potentially offer a means to control the porous structure, including pore size and density.

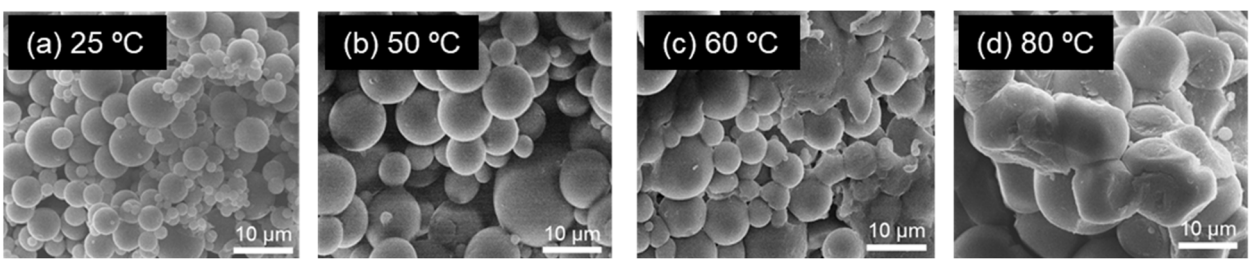

Fig. 4 SEM images of aluminate porous microbeads prepared by aging at (a) 25 °C, (b) 50 °C, (c) 60 °C and (d) 80 °C.

The formation mechanism of porous aluminate microbeads

We hypothesize that the extraction of ethanol from droplets to external oil phase drives the formation of microbeads observed in the current process. To verify this, the transport of ethanol was comparatively examined in the cases of using two oil phases, dodecane and toluene. Fig. 5a shows the three-dimensional Hansen solubility parameter centered on ethanol. The Hansen solubility parameter is an index used to evaluate the affinity between solvents. Generally, the closer the distance (R_a) of a given solvent to the central solvent (ethanol in the present case), the higher the affinity between the two solvents.[41] When ethanol is the central solvent, $R_a = 5.33$ for dodecane and 4.85 for toluene. Hansen parameter suggests that ethanol has a higher affinity for toluene than for dodecane. The synthesis of microbeads with toluene and dodecane as oil phases was performed to tune the speed of ethanol extraction from the droplets. Fig. 5b shows a SEM image of microbeads synthesized using toluene as the oil phase. Microbeads were not obtained when toluene was used as the oil phase, in contrast to the case with using dodecane. In the case of using toluene, excessive ethanol was extracted to the oil (toluene) phase from the aqueous phase, preventing emulsification. On the other hand, in the case of using dodecane, it is suggested that an extraction from aqueous phase of ethanol to oil (dodecane) phase caused a moderate loss of dispersion stability of the aluminum hydroxide nanoparticle in the aqueous phase, resulting in the formation of microbeads. While the interfacial environment is complex due to the presence of surfactants and concentrated nanoparticles, the HSP serves as a useful indicator of the thermodynamic driving force for alcohol transport.

The interaction between water and ethanol is an important factor in the successful extraction of ethanol when dodecane is used as the oil phase. Either oil phase (dodecane and toluene) was gently poured on the dispersion of aluminum hydroxide nanoparticle to form macroscopic two-phase separation. Then, the two-phase-separated liquid was aged at room temperature. Fig. 5c and d show the FT-IR spectra of oil phases after aging. When using dodecane as the oil phase, apparent spectral change was not observed in 24 h. On the other hand, using toluene as the oil phase resulted in the appearance of absorption peaks derived from ethanol at 2976 and 3380 cm^{-1} over time.[37] This indicates that ethanol is significantly extracted to the oil phase in the case of toluene because ethanol has a higher affinity for toluene than dodecane. The limited extraction of ethanol to dodecane phase was further investigated. Either ethanol or a mixture of water/ethanol was poured onto dodecane to form two-phase-separated system and then the changes in the chemical species in each oil phase were analyzed. Fig. S4

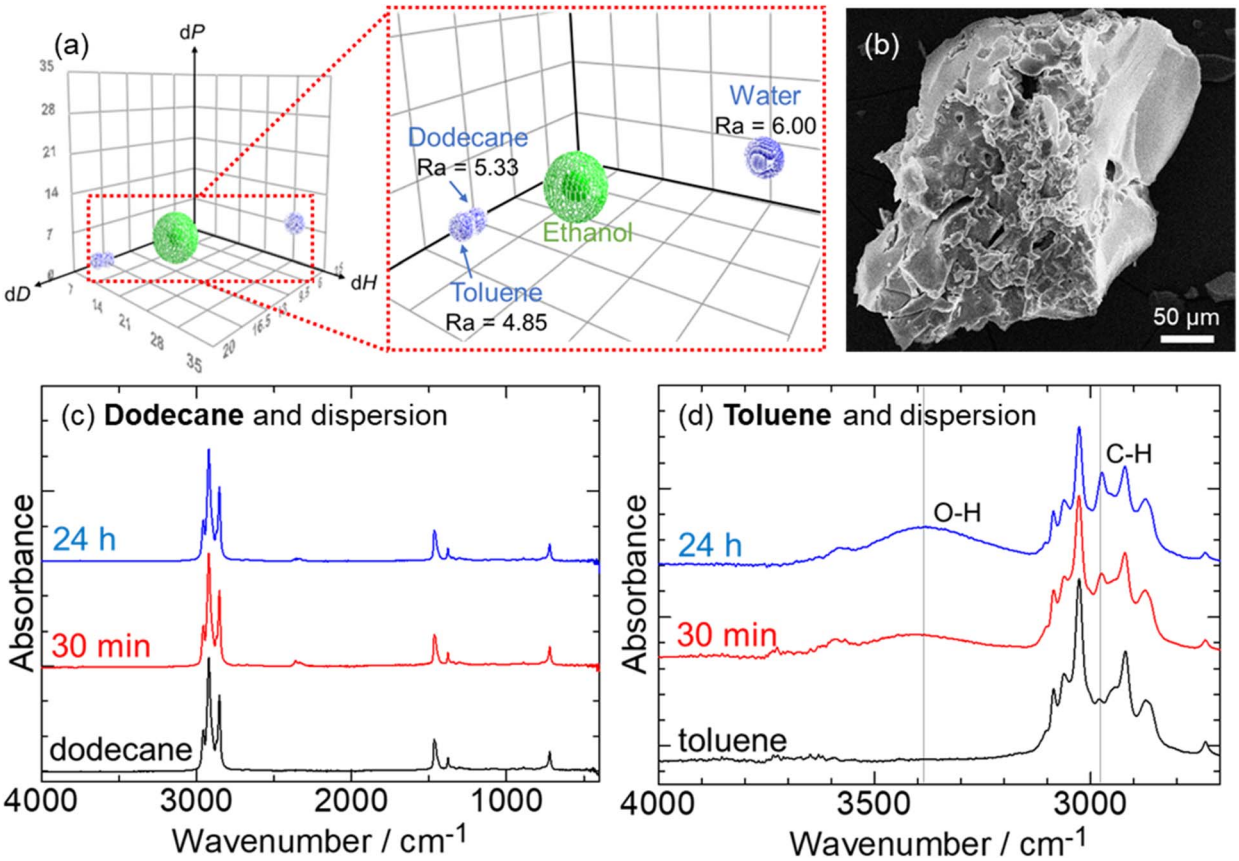

Fig. 5 (a) Three-dimensional Hansen solubility parameter centered on ethanol. Three axes correspond to contributions influencing on intermolecular interaction; dD: dispersion force; dP: polar force; dH: hydrogen bonding. (b) SEM image of aluminate microbeads prepared with toluene as the oil phase. FT-IR spectra of the oil phase after aging for (c) dodecane and dispersion, and (d) toluene and dispersion.

shows the FT-IR spectra of each oil phase after aging. Pure ethanol (Fig. S4a) rapidly transports to dodecane as the peaks derived from ethanol were observed in 5 min. While ethanol showed retarded extraction in the presence of water (Fig. S4b) and no apparent peaks derived from ethanol were observed even after 24 h. The result suggests that water in the aqueous phase control the speed of ethanol extraction to oil phase. We can conclude that the successful formation of porous aluminate microbeads in the case of dodecane is due to relatively slow and homogenous extraction of ethanol thanks to partition of ethanol between water and dodecane.

Conclusions

Porous aluminate microbeads have been successfully synthesized from emulsion droplets containing nanoparticle with an average diameter of 5.8 nm under the optimized conditions. The microbeads had a particle size with an average diameter of 7.5 μm and micropores with an average diameter of 1.8 nm. The microbeads showed microporosity showing a high specific surface area of 430 m^2 g^{-1}. The mechanism of microbead formation was elucidated. Extraction of ethanol from aqueous droplets to surrounding oil phase drives the formation of microbeads in the current process. When dodecane is used as the oil phase, the interaction between water and ethanol regulates the rate of ethanol extraction to a moderate level. The partition of ethanol between water and dodecane also allows for relatively slow and homogeneous extraction of ethanol. The concept demonstrated in this study provides a potential platform for the synthesis of porous microbeads across various inorganic systems starting from similar nanoparticle dispersions.

Author contributions

Conceptualization: Y. T.; investigation: S. K., and M. I.; writing (original draft): S. K.; writing (review and editing): Y. T., K. O., and A. N.; funding acquisition: Y. T., and A. N.; validation: S. K.

Conflicts of interest

The authors declare no competing financial interest.

Data availability

The authors confirm that the data supporting the findings of this study are available within the article and its supplementary information (SI). Supplementary information is available. See DOI: https://doi.org/10.1039/d6ra03388a.

Acknowledgements

The present work was partly supported by JSPS KAKENHI (Grant Numbers JP24K01165, JP24K21812, and JP24KK0204) and the Nippon Sheet Glass Foundation for Materials Science and Engineering. The authors thank Dr Norio Ishizuka (Emaus Kyoto, Inc., Japan) for his technical support with the synthesis.

References

1 C. S. Guo, M. Ge, L. Liu, G. Gao, Y. Feng and Y. Wang, *Environ. Sci. Technol.*, 2010, **44**(1), 419–425.
2 Z. Wu, K. Yu, S. Zhangand and Y. Xie, *J. Phys. Chem. C*, 2008, **112**(30), 11307–11313.
3 A. Armutlulu, M. A. Naeem, H. J. Liu, S. M. Kim, A. Kierzkowska, A. Fedorov and C. R. Muller, *Adv. Mater.*, 2017, **41**, 6–29.
4 J. M. Anderson and M. S. Shive, *Adv. Drug Deliv. Rev.*, 2012, **64**, 72–82.
5 V. R. Sinha, A. K. Singla, S. Wadhawan, R. Kaushik, R. Kumria, K. Bansal and S. Dhawan, *Int. J. Pharm.*, 2004, **274**, 1–33.
6 Y. Qiu, Y. Lin, H. Yang, L. Wang, M. Wang and B. Wen, *Chem. Eng. J.*, 2020, **383**, 123207.
7 Y. Xia, Z. Xiao, X. Dou, H. Huang, X. Lu, R. Yan, Y. Gan, W. Zhu, J. Tu, W. Zhang and X. Tao, *ACS Nano*, 2013, **7**(8), 7083–7092.
8 Y. Zhang, K. Ruan, K. Zhou and J. Gu, *Adv. Mater.*, 2023, **35**, 2211642.
9 S. Xuan, W. Jiang, X. Gong, Y. Hu and Z. Chen, *J. Phys. Chem. C*, 2009, **113**(2), 553–558.
10 Z. Wang, Y. Chen, L. Zhang, B. Cheng, J. Yu and J. Fan, *J. Mater. Sci. Technol.*, 2020, **56**, 143–150.
11 S. Fujii, M. Oleada, H. Sawa, T. Furuzono and Y. Nakamura, *Langmuir*, 2009, **25**(17), 9759–9766.
12 Y. Yang, Z. Fang, X. Chen, W. Zhang, Y. Xie, Y. Chen, Z. Liu and W. Yuan, *Front. Pharmacol*, 2017, (8), 287.
13 C. Y. Gao, M. W. Kim, D. H. Bae, Y. Z. Dong, S. H. Piao and H. J. Choi, *Polymer*, 2017, **125**, 21–29.
14 Z. L. Liu, Z. H. Ding, K. L. Yao, J. Tao, G. H. Du, Q. H. Lu, X. Wang, F. L. Gong and X. Chen, *J. Magn. Magn. Mater.*, 2003, **265**(1), 98–105.
15 A. Hanprasopwattana, S. Srinivasan, A. G. Sault and A. K. Datye, *Langmuir*, 1996, **13**(12), 3173–3179.
16 A. J. Fijneman, J. Högblom, M. Palmlöf, G. de With, M. Persson and H. Friedrich, *Adv. Funct. Mater.*, 2020, **30**(27), 2002725.
17 N. Andersson, R. W. Corkery and P. C. A. Alberius, *J. Mater. Chem.*, 2007, **17**(26), 2700–2705.
18 S. H. Kim, Y. S. Cho, S. J. Jeon, T. H. Eun, G. R. Yi and S. M. Yang, *Adv. Mater.*, 2008, **20**(17), 3268–3273.
19 D. F. F. Brossault, T. M. McCoy and A. F. Routh, *J. Colloid Interface Sci.*, 2021, **584**, 779–788.
20 L. H. Allen and E. Matihevic, *J. Colloid Interface Sci.*, 1969, **31**(3), 287–296.
21 K. Higashitani, M. Kondo and S. Hatade, *J. Colloid Interface Sci.*, 1991, **142**(1), 204–213.
22 Y. Tokudome, T. Morimoto, N. Tarutani, P. D. Vaz, C. D. Nunes, V. Prevot, G. B. G. Stenning and M. Takahashi, *ACS Nano*, 2016, **10**(5), 5550–5559.
23 Y. Tokudome, A. Koyama, H. Murata, K. Okada, A. Nakahira, S. Nishimura, M. Takahashi and J. Solgel, *Sci. Technol.*, 2022, **104**(3), 580–587.
24 D. Kino, Y. Tokudome, P. D. Vaz, C. D. Nunes and M. Takahashi, *Asian. Ceram. Soc.*, 2017, **5**(4), 466–471.

25 M. Takemoto, Y. Tokudome, H. Murata, K. Okada, M. Takahashi and A. Nakahira, *Appl. Clay Sci.*, 2021, **203**, 106006.
26 N. Tarutani, Y. Tokudome, M. Jobbágy, G. J. A. A. Soler-Illia, Q. Tang, M. Müller and M. Takahashi, *Chem. Mater.*, 2019, **31**(2), 322–330.
27 A. Amimoto, Y. Tokudome, A. Obata, S. Ibayashi, N. Tarutani, R. Shinchi and A. Nakahira, *Mater. Chem. Phys.*, 2025, **344**, 131132.
28 Y. Tokudome, Y. Ando, K. Yoneda, S. Takeda, A. Takabatake, N. Tarutani and A. Nakahira, *Langmuir*, 2025, **41**(13), 8545–8553.
29 F. Bai, D. Wang, Z. Huo, W. Chen, L. Liu, X. Liang, *et al.*, *Angew. Chem., Int. Ed.*, 2007, **46**(35), 6650–6653.
30 A. E. Gash, T. M. Tillotson, J. H. Satcher, J. F. Poco, L. W. Hrubesh and R. L. Simpson, *Chem. Mater.*, 2001, **13**(3), 999–1007.
31 Y. Tokudome, *JCS-Japan*, 2017, **125**, 597–602.
32 J. T. Kloprogge, L. Hickey and R. L. Frost, *JRS*, 2004, **35**(11), 967–974.
33 R. Botan, T. R. Nogueira, F. Wypych and L. M. F. Lona, *Polym. Eng. Sci.*, 2012, **52**(8), 1754–1760.
34 R. L. Frost, J. Kloprogge, S. C. Russell and J. L. Szetu, *Thermochim. Acta*, 1999, **329**(1), 47–56.
35 F. Li, J. Liu, D. G. Evans and X. Duan, *Chem. Mater.*, 2004, **16**(8), 1597–1602.
36 K. Nishio, T. Sei and T. Tsuchiya, *Mater. Sci.*, 1996, **31**, 1761–1766.
37 A. J. Barnes and H. E. Hallam, *Trans. Faraday. Soc.*, 1970, **66**, 1932–1940.
38 H. J. Chen, L. Wang and W. Y. Chiu, *Mater. Chem. Phys.*, 2007, **101**(1), 12–19.
39 Y. Tokudome, K. Nakanishi, K. Kanamori, K. Fujita, H. Akamatsu and T. Hanada, *J. Colloid Interface Sci.*, 2009, **338**(2), 506–513.
40 Y. Tokudome, M. Fukui, N. Tarutani, S. Nishimura, V. Prevot, C. Forano, *et al.*, *Langmuir*, 2016, **32**(35), 8826–8833.
41 C. M. Hansen, *Ind. Eng. Chem. Prod. Res. Dev.*, 1969, **8**(1), 2–11.